

Data-driven high-fidelity prediction of the equivalent sand-grain height of rough surfaces

Mostafa Aghaei Jouybari¹†, Junlin Yuan¹‡ and Giles J. Brereton¹¶

¹Department of Mechanical Engineering, Michigan State University, East Lansing, MI 48824, USA

(Received xx; revised xx; accepted xx)

This work addresses a long standing question about roughness: what is the equivalent sand-grain height, given the roughness topography? Deep Neural Network (DNN) and Gaussian Process Regression (GPR) machine learning approaches are used to develop a high-fidelity prediction approach of the Nikuradse equivalent sand-grain height k_s (Nikuradse 1933) for turbulent flows over a wide variety of different rough walls. To this end, 45 surface geometries are generated and simulated at $Re_\tau = 1000$. The surfaces geometry differ widely in moments of surface height fluctuations, effective slope, average inclination, porosity and degree of randomness. When combined with 15 fully rough experimental data sets, courtesy of Flack et al (Flack *et al.* 2016; Barros *et al.* 2018; Flack *et al.* 2019), the DNN and GPR methods predict k_s with an rms error of less than 10% and a maximum error of less than 30%, which appears to be significantly more accurate than existing correlations applied to the present database.

1. Introduction

At sufficiently high Reynolds numbers, all surfaces are hydrodynamically rough, as is almost always the case for flows past the surfaces of naval vehicles. Reviews of roughness effects on wall-bounded turbulent flows are provided by Raupach *et al.* (1991) and Jiménez (2004). The most important effect of surface roughness in engineering applications is an increase in the hydrodynamic drag (Flack 2018), which is due predominantly to the pressure drag generated by the small-scale recirculation regions associated with individual roughness protuberances.

For the foreseeable future, the most practical approach to making predictive flow calculations at realistic naval operating conditions is to use engineering one-point closure models of turbulence, such as two-equation turbulent eddy viscosity closures for the Reynolds-averaged Navier-Stokes (RANS) equations. Existing rough-wall corrections to this type of closure typically model the increase in hydrodynamic drag on a single length scale—the equivalent sand-grain height (Nikuradse 1933) k_s —without physically resolving the surface or changing the governing equations. In the fully rough flow regime, where the wall friction depends on the roughness alone and is independent of the Reynolds number, k_s quantifies the increase in hydrodynamic drag through an empirical relation with the roughness function ΔU^+ ,

$$\Delta U^+ = \frac{1}{\kappa} \ln k_s^+ - 3.5, \quad (1.1)$$

† Email address for correspondence: aghaeijo@egr.msu.edu

‡ Email address for correspondence: junlin@egr.msu.edu

¶ Email address for correspondence: brereton@egr.msu.edu

where $\kappa = 0.41$ is von Kármán's constant, $+$ represents normalization in wall units, and ΔU^+ is defined as the offset of the log-linear velocity profile of a rough-wall flow relative to that of a smooth-wall one, and represents the increase in drag due to surface roughness.

Since k_s is a flow-dependent roughness lengthscale, rather than a physical one, it is not known a priori and does not appear to be equivalent to any single geometrical length scale, such as an average or a root-mean-square (rms) of roughness height (Flack 2018). It is also well-established that k_s can depend on many geometrical parameters such as the effective slope (Napoli *et al.* 2008; Yuan & Piomelli 2014a) and the skewness of the roughness height distribution (Flack & Schultz 2010). Readers are referred to Flack & Schultz (2010) and Bons (2002) for extensive reviews on this topic. Empirical expressions for k_s based on a small number of geometrical roughness parameters have been proposed in several studies. Examples of existing empirical correlations are

$$k_s = c_1 k_{avg} (\alpha_{rms}^2 + c_2 \alpha_{rms}), \quad (1.2)$$

proposed by Bons *et al.* (2001),

$$k_s = c_1 k_{avg} \Lambda_s^{c_2}, \quad (1.3)$$

proposed by van Rij *et al.* (2002) and

$$k_s = c_1 k_{rms} (1 + skw)^{c_2}, \quad (1.4)$$

given by Flack & Schultz (2010). Here, k_{avg} is the averaged height, α is the local streamwise slope angle and $\Lambda_s = (S/S_f)(S_f/S_s)^{-1.6}$, where S , S_f , S_s are different reference areas. k_{rms} and skw are rms and skewness of the roughness height fluctuations. c_1 , c_2 are constants.

The hydrodynamic lengthscale k_s appears to be correlated with different sets of geometrical parameters for different types of rough surface and no universal correlation currently exists for flow over surfaces of arbitrary roughness. For example, for synthetic roughness comprising closely packed pyramids (Schultz & Flack 2009) and random sinusoidal waves (Napoli *et al.* 2008), it has been shown that k_s scales on the effective slope when the surface slope is mild (i.e. within the 'waviness' regime), whereas the skewness and rms height, but *not* slope magnitude, become important when the slope is intense (i.e. within the 'roughness' regime). The boundary between these two regimes has also been shown to be surface dependent (Yuan & Piomelli 2014a).

In previous studies, the small number of roughness parameters used to devise k_s correlations tended to limit their application to a narrow range of surface roughnesses. Since it appears that many geometrical parameters, such as porosity, moments of roughness height (e.g. rms, skewness and kurtosis), effective slope, and surface inclination angle might affect k_s , it is useful to employ a data science approach suited to modeling large multi-variate/multi-output systems. In particular, we use Machine Learning (ML) to explore k_s -prediction approaches that depend on a large set of surface-topographical parameters, with the expectation that the resulting models may be applied accurately to a wider range of surfaces. The extensive computational and experimental data sets available on k_s , for a wide range of surface roughnesses, are well suited to the requirements of ML.

Since the prediction of k_s from surface topography lengthscales is essentially a 'labeled' regression problem, supervised ML operations were performed, using deep neural networks (DNN), Gaussian process regressions (GPR) and support vector machines (SVM). Readers are referred to the monogram by Géron (2017) and the review provided by LeCun *et al.* (2015) for in-detail discussions about the methods. All these three ML methods

were applied. The major expense in this exercise is the generation and collection of data, rather than evaluating and comparing the performance of various ML procedures per se. The results obtained using the DNN and GPR approaches are reported in this paper; our preliminary effort with SVM did not provide as accurate prediction as the other two approaches. An initial collection of 60 sets of data on k_s as a function of topographical parameters—45 DNS results and 15 experimental results—are considered. All experimental data sets are fully-rough and within DNS data, 30 of them are identified as fully-rough flows and are used for ML training and testing.

The paper is organized as follows. We first describe the governing equations, solution methodologies, simulation parameters and different roughness topographies. Then, the post-processing of DNS results to calculate k_s is presented. Finally, we show the ML model predictions for k_s and discuss the prediction uncertainty.

2. Problem formulation

2.1. Governing equations

The governing equations of incompressible continuity and linear momentum—the Navier-Stokes (NS) equations—for a constant-property Newtonian fluid, were solved using direct numerical simulation (DNS). These equations are written in indicial notation as

$$\frac{\partial u_i}{\partial x_i} = 0, \quad (2.1a)$$

$$\frac{\partial u_i}{\partial t} + \frac{\partial u_i u_j}{\partial x_j} = -\frac{\partial P}{\partial x_i} + \nu \frac{\partial^2 u_i}{\partial x_j \partial x_j} + F_i, \quad (2.1b)$$

Here, $i, j = 1, 2, 3$, x_1, x_2 and x_3 (or x, y, z) are the streamwise, wall-normal and spanwise coordinates, with corresponding velocity components of u_1, u_2 and u_3 (or u, v, w) and P is defined as p/ρ , ρ is the fluid density and ν is the kinematic viscosity. An immersed boundary method (Scotti 2006) was used to enforce the fine-grained roughness boundary conditions on a non-conformal Cartesian grid. The corresponding body force F_i is added to the the right hand side of the momentum equations to impose a no-slip boundary condition at the fluid-roughness interface. To solve the equations, second-order central differencing was used for spatial discretizations and second-order Adams-Bashforth semi-implicit time advancement was employed. The numerical solver was paralleled using the message passing interface (MPI) method (Keating 2004).

A double-averaging decomposition (Raupach & Shaw 1982) was used to resolve turbulent and dispersive components of flow variables in the presence of roughness. In this decomposition, any instantaneous flow variable θ may be decomposed into three components, as

$$\theta(\mathbf{x}, t) = \langle \bar{\theta} \rangle(y) + \theta'(\mathbf{x}, t) + \tilde{\theta}(\mathbf{x}) \quad (2.2)$$

where the time-averaging operator is $\bar{\theta}$ and the intrinsic spatial-averaging operator is $\langle \theta \rangle = \frac{1}{A_f} \int_{x,z} \theta dA$ (and A_f is the area occupied by fluid). The Reynolds and dispersive fluctuating components are then $\theta' = \theta - \bar{\theta}$ and $\tilde{\theta} = \bar{\theta} - \langle \bar{\theta} \rangle$ respectively.

The calculation of wall shear stress (including both viscous and pressure drag contributions on a rough wall) is by integrating the time-averaged immersed boundary method body force in x , F_1 ,

$$\tau_w = \frac{\rho}{L_x L_z} \int_{\mathcal{V}} \bar{F}_1(x, y, z) dx dy dz, \quad (2.3)$$

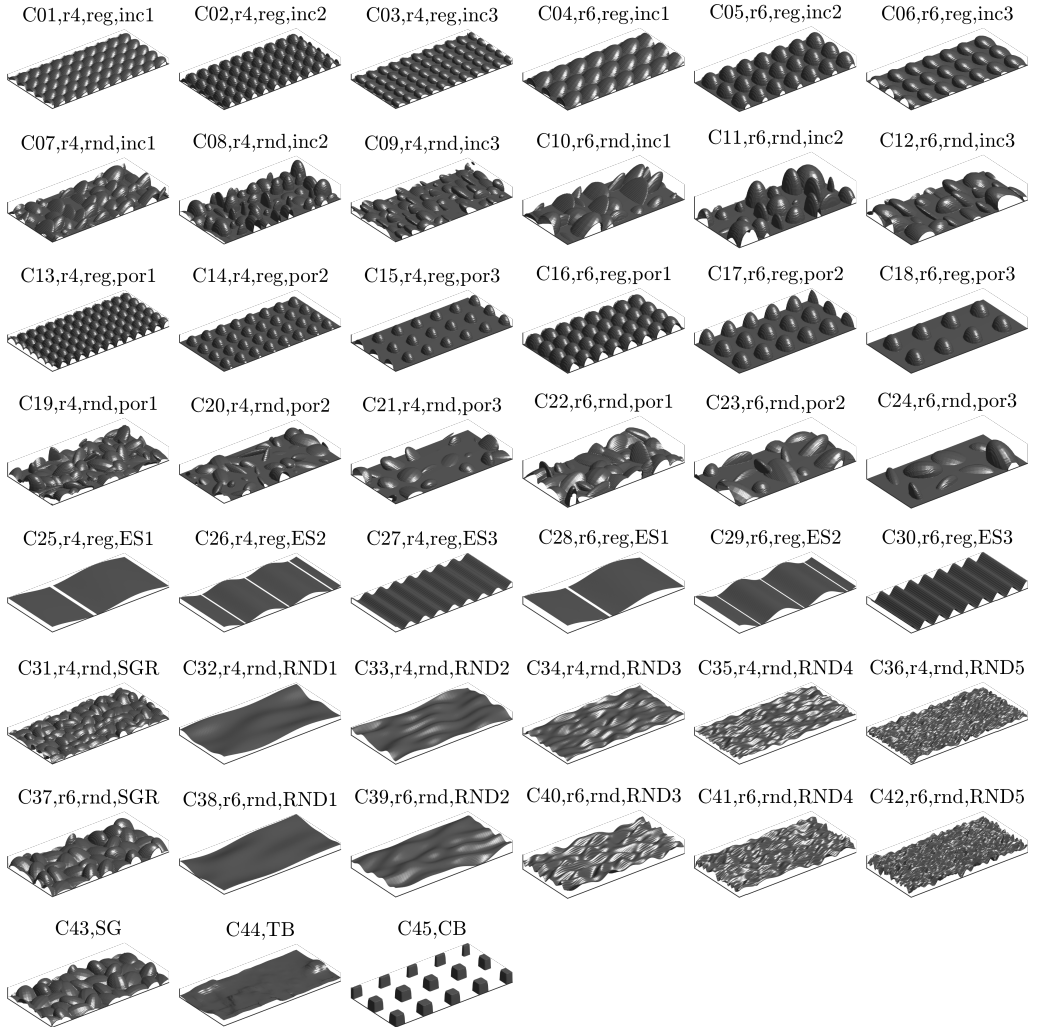


FIGURE 1. Roughness geometries.

where \mathcal{V} represents the total simulation domain below the roughness crest and L_{x_i} is the domain size in x_i direction. Readers are referred to Yuan & Piomelli (2014*b,c*) for details of the implementation and validation of the immersed boundary method and τ_w calculation.

2.2. Surface roughness

In Figure 1, the 45 roughness geometries used for the present DNS are displayed. Each case name in Figure 1 consists of a letter denoting computational (“C”) or experimental (“E”) data and an index assigned to each surface. For computational cases, the names also have a lengthscale (a percentage of δ) used in generation of that surface, the regular (“reg”) or random (“rnd”) type of the surface, and the feature that was varied to create that particular surface as one of a series. These features were: the streamwise inclination angle (inc_x) in surfaces C01 to C12; the porosity (por) in surfaces C13 to C24; and the streamwise effective slope (ES_x) in surfaces C25 to C30. For experimental cases two sets of other numbers are assigned to each surface (see table 1). The first one denotes the

Case name	k_{avg}	k_c	k_{rms}	Ra	inc_x	inc_z	por	ES_x	ES_z	skw	kur	k_s
C01,r4,reg,inc1	0.0258	0.0425	0.0128	0.0108	-0.8014	-0.0858	0.5352	0.5837	0.5094	-0.5439	2.1768	
C02,r4,reg,inc2	0.0304	0.0592	0.0211	0.0186	0.0117	0.0323	0.6087	1.0294	0.5615	-0.2648	1.5969	
C03,r4,reg,inc3	0.0250	0.0425	0.0130	0.0110	0.8208	-0.0779	0.5374	0.6000	0.4852	-0.4588	2.0522	
C04,r6,reg,inc1	0.0322	0.0642	0.0219	0.0194	-0.9779	0.0161	0.5971	0.5949	0.5900	-0.1671	1.6007	0.064
C05,r6,reg,inc2	0.0376	0.0877	0.0326	0.0298	0.0245	0.0642	0.6535	0.9158	0.6427	0.1093	1.4355	0.124
C06,r6,reg,inc3	0.0311	0.0642	0.0218	0.0193	0.9552	0.1214	0.5989	0.5876	0.5583	-0.0874	1.5898	0.059
C07,r4,rnd,inc1	0.0248	0.0860	0.0223	0.0190	-0.8595	0.0325	0.7736	0.5114	0.5594	0.5600	2.2435	0.094
C08,r4,rnd,inc2	0.0273	0.1161	0.0298	0.0254	-0.0072	0.0482	0.8191	0.8612	0.6044	0.8702	2.6269	0.217
C09,r4,rnd,inc3	0.0250	0.0828	0.0214	0.0181	0.8289	0.0023	0.7529	0.5168	0.4822	0.5141	2.2923	0.174
C10,r6,rnd,inc1	0.0256	0.1250	0.0298	0.0253	-0.9568	-0.0192	0.8351	0.4979	0.5784	0.9671	2.8736	0.188
C11,r6,rnd,inc2	0.0333	0.1724	0.0437	0.0367	0.0759	0.1382	0.8416	0.7579	0.5429	1.1501	3.1762	0.354
C12,r6,rnd,inc3	0.0318	0.1273	0.0315	0.0266	0.9232	0.0317	0.7837	0.5076	0.4713	0.7575	2.6415	0.185
C13,r4,reg,por1	0.0378	0.0592	0.0182	0.0151	0.0243	0.0656	0.4975	1.0430	0.5228	-0.8199	2.5081	
C14,r4,reg,por2	0.0176	0.0592	0.0217	0.0197	0.0208	0.0378	0.7763	0.6130	0.4559	0.7078	1.8403	0.141
C15,r4,reg,por3	0.0096	0.0592	0.0182	0.0143	0.0224	0.0630	0.8770	0.3337	0.2526	1.6456	4.0941	0.157
C16,r6,reg,por1	0.0506	0.0893	0.0304	0.0262	0.0409	0.1494	0.5289	1.1370	0.5343	-0.5377	1.8731	0.077
C17,r6,reg,por2	0.0220	0.0893	0.0310	0.0274	0.0406	0.0796	0.8012	0.5372	0.4027	0.9822	2.3078	0.260
C18,r6,reg,por3	0.0126	0.0893	0.0259	0.0195	0.0567	0.1255	0.8857	0.3068	0.2302	1.8486	4.8394	0.247
C19,r4,rnd,por1	0.0269	0.1119	0.0207	0.0166	0.0249	-0.1068	0.8058	0.4870	0.4862	0.7322	3.4216	0.102
C20,r4,rnd,por2	0.0127	0.0946	0.0169	0.0139	0.0324	-0.6456	0.8961	0.3108	0.3232	1.3431	4.1256	0.132
C21,r4,rnd,por3	0.0089	0.0982	0.0161	0.0120	0.3209	-0.7409	0.9292	0.2189	0.2329	2.1683	7.7277	0.089
C22,r6,rnd,por1	0.0345	0.1393	0.0287	0.0239	-0.0696	-0.2453	0.7909	0.4556	0.4986	0.5910	2.8296	0.212
C23,r6,rnd,por2	0.0173	0.1227	0.0249	0.0202	-0.6719	-0.8405	0.8848	0.3046	0.3252	1.4673	4.3466	0.177
C24,r6,rnd,por3	0.0135	0.1523	0.0265	0.0190	0.1890	-0.0560	0.9263	0.2542	0.2573	2.3707	8.7396	0.123
C25,r4,reg,ES1	0.0202	0.0399	0.0140	0.0126	0.0457	0.0061	0.5097	1.0603	0.0086	-0.0323	1.5026	
C26,r4,reg,ES2	0.0207	0.0399	0.0139	0.0126	0.0390	-0.0012	0.5098	0.2124	0.0195	-0.0712	1.5051	0.065
C27,r4,reg,ES3	0.0226	0.0399	0.0135	0.0122	0.0056	-0.0225	0.5102	0.6092	0.0317	-0.2140	1.5443	
C28,r6,reg,ES1	0.0304	0.0592	0.0210	0.0190	0.0443	0.0182	0.5041	1.1581	0.0145	-0.0308	1.4991	0.071
C29,r6,reg,ES2	0.0311	0.0592	0.0210	0.0189	0.0282	-0.0687	0.5041	0.3162	0.0222	-0.0709	1.5031	0.112
C30,r6,reg,ES3	0.0339	0.0592	0.0203	0.0182	0.0145	-0.0688	0.5045	0.9168	0.0479	-0.2033	1.5426	0.064
C31,r4,rnd,SGR	0.0253	0.0592	0.0114	0.0093	0.1038	-0.0389	0.6477	0.3704	0.3982	0.3777	2.7840	0.049
C32,r4,rnd,RND1	0.0404	0.0751	0.0130	0.0103	0.1165	0.1084	0.4789	0.0680	0.1691	-0.0694	2.9905	
C33,r4,rnd,RND2	0.0412	0.0877	0.0130	0.0105	0.1087	0.0779	0.5528	0.1170	0.3084	0.0041	2.7634	
C34,r4,rnd,RND3	0.0420	0.0796	0.0098	0.0078	0.0697	0.0510	0.5078	0.1750	0.4577	-0.0017	3.0309	
C35,r4,rnd,RND4	0.0428	0.0766	0.0082	0.0066	0.0392	0.0417	0.4882	0.2183	0.5576	0.0127	2.9409	
C36,r4,rnd,RND5	0.0453	0.0844	0.0089	0.0071	0.0350	0.0372	0.5354	0.3778	0.8410	0.0749	3.0179	
C37,r6,rnd,SGR	0.0369	0.0877	0.0184	0.0149	0.3119	0.1799	0.6401	0.4280	0.4628	0.0321	2.6859	0.109
C38,r6,rnd,RND1	0.0604	0.1059	0.0156	0.0123	0.0450	0.0283	0.4440	0.0770	0.1834	-0.2196	3.2577	
C39,r6,rnd,RND2	0.0609	0.0982	0.0117	0.0093	0.1107	0.0569	0.4004	0.1081	0.2847	-0.0199	3.2670	
C40,r6,rnd,RND3	0.0635	0.1205	0.0162	0.0129	0.0609	0.0220	0.5115	0.2803	0.7596	0.0372	2.9768	0.050
C41,r6,rnd,RND4	0.0651	0.1296	0.0145	0.0115	0.0448	0.0368	0.5457	0.3740	0.9887	0.0279	3.0362	
C42,r6,rnd,RND5	0.0676	0.1183	0.0126	0.0101	0.0373	0.0253	0.5029	0.5474	1.2042	0.0516	2.9325	
C43,SG	0.0359	0.0889	0.0171	0.0137	0.2882	0.1557	0.6492	0.4252	0.4405	0.4758	2.9703	0.093
C44,TB	0.0552	0.1245	0.0184	0.0142	0.0070	-0.0060	0.5694	0.0967	0.0810	0.2001	3.4927	0.024
C45,CB	0.0098	0.0695	0.0228	0.0159	0.4200	0.5084	0.8781	0.2493	0.2465	2.1006	5.5686	0.150
E01,16,2	0.1380	0.2605	0.0204	0.0161	-0.0052	0.0114	0.4716	0.7202	0.8354	-0.7109	3.8425	0.052
E02,16,3	0.1434	0.2518	0.0205	0.0164	-0.0211	0.0099	0.4320	0.7401	0.8675	-0.3380	3.1589	0.050
E03,16,7	0.1326	0.3649	0.0185	0.0141	-0.0380	-0.0004	0.6375	0.6177	0.7050	-1.1689	5.2921	0.058
E04,16,8	0.1259	0.2984	0.0165	0.0127	-0.0338	0.0088	0.5791	0.5870	0.6819	-1.4448	5.4214	0.056
E05,16,9	0.1123	0.3084	0.0175	0.0139	-0.0306	0.0150	0.6367	0.6362	0.7528	-0.7384	3.7139	0.043
E06,16,15	0.0809	0.1909	0.0126	0.0098	-0.0266	0.0029	0.5775	0.6209	0.7128	-0.6874	3.8541	0.035
E07,18,1	0.1206	0.2406	0.0264	0.0211	-0.0129	-0.1832	0.4999	0.1810	0.1881	0.1074	2.9405	0.053
E08,18,2	0.1430	0.2760	0.0318	0.0254	-0.0193	0.1939	0.4832	0.1624	0.1644	0.0934	2.9670	0.034
E09,19,1	0.2102	0.4692	0.0449	0.0360	0.0175	-0.0466	0.5532	0.2286	0.2342	-0.0729	2.9554	0.065
E10,19,2	0.3887	0.7627	0.0877	0.0702	0.0463	0.0015	0.4916	0.4466	0.4521	-0.0651	2.9253	0.200
E11,19,3	0.4772	0.7301	0.0881	0.0704	-0.0289	-0.2449	0.3480	0.4336	0.4317	-0.6595	3.2739	0.160
E12,19,4	0.4585	0.7513	0.0885	0.0708	-0.0522	0.0363	0.3913	0.4551	0.4585	-0.3512	3.0406	0.180
E13,19,5	0.2922	0.7316	0.0895	0.0715	-0.0582	-0.0044	0.6016	0.4448	0.4524	0.3458	3.0505	0.245
E14,19,6	0.2022	0.7109	0.0866	0.0692	0.0035	-0.0101	0.7163	0.3909	0.4003	0.8117	3.5588	0.435
E15,19,7	0.5216	0.9673	0.1142	0.0920	-0.0499	-0.2347	0.4621	0.5569	0.5621	-0.0662	2.7937	0.230

TABLE 1. Statistical parameters of roughness topography and the equivalent sand-grain height k_s .

year of the publication that the surface was used in; surfaces with number 16 are from Flack *et al.* (2016), with number 18 are from Barros *et al.* (2018) and with number 19 are from Flack *et al.* (2019). The second number is the index that the surface have been assigned in the original paper.

Surfaces C01 through C24 were created using ellipsoidal elements (Scotti 2006) of different size, aspect ratio and inclination. For *regular* roughness, each element has the same orientation and semi-axis lengths, $(\lambda_1, \lambda_2, \lambda_3) = (1.0, 0.7, 0.5)k_c$, following Scotti (2006). For *random* roughness, the elements have random orientations and semi-axis lengths (with uniform distributions of the random variables). The average orientation and semi-axis lengths are the same as the corresponding *regular* surface. Surfaces C25 through C30 comprise sinusoidal waves in the x direction, of the same magnitude but different wavelengths to generate different values of effective slope ES_x . The wavelengths were $\lambda_{r,x} = 3\delta/4$, $3\delta/8$ and $\delta/6$. Surfaces C31 and C37 comprise the random sand-grain roughness of Scotti (2006), which were produced by randomly oriented ellipsoidal elements with fixed semi-axes of $(1.0, 0.7, 0.5)k_c$. Surfaces C32 through C36 and C38 through C42 were generated as the low-order (the first 5, 10, 20, 30 and 50) modes of Fourier transforms of white noise in the streamwise and spanwise directions; they therefore describe random surfaces with large to small wavelength roughness. Cases C43, C44 and C45 are DNS (full-span channel) of flow over a random sand-grain roughness, a realistic turbine-blade roughness scan, and arrays of cubes. These surfaces were used in the study of Aghaei Jouybari *et al.* (2019). Case C46 is the reference case of a smooth-wall flow.

Other surface parameters calculated for each surface in this work and tabulated in table 1 include the mean roughness height (k_{avg}), the first-order moment of height fluctuations (Ra), the root-mean-square of roughness height (k_{rms}), the roughness height skewness (skw) and its kurtosis (kur), the effective slope in the x_i direction (ES_{x_i}), and the inclination angle (in radians) in the x_i direction (inc_{x_i}), together with the hydrodynamic lengthscale k_s deduced from the mean velocity field using Equation (1.1). The definitions of these geometrical parameters are summarized as the following:

$$k_{avg} = \frac{1}{A_t} \int_{x,z} k dA, \quad (2.4)$$

$$Ra = \frac{1}{A_t} \int_{x,z} (|k - k_{avg}|) dA, \quad (2.5)$$

$$k_{rms} = \sqrt{\frac{1}{A_t} \int_{x,z} (k - k_{avg})^2 dA}, \quad (2.6)$$

$$skw = \frac{1}{A_t} \int_{x,z} (k - k_{avg})^3 dA / k_{rms}^3, \quad (2.7)$$

$$kur = \frac{1}{A_t} \int_{x,z} (k - k_{avg})^4 dA / k_{rms}^4, \quad (2.8)$$

$$ES_x = \frac{1}{A_t} \int_{x,z} \left| \frac{\partial k}{\partial x} \right| dA, \quad (2.9)$$

$$ES_z = \frac{1}{A_t} \int_{x,z} \left| \frac{\partial k}{\partial z} \right| dA, \quad (2.10)$$

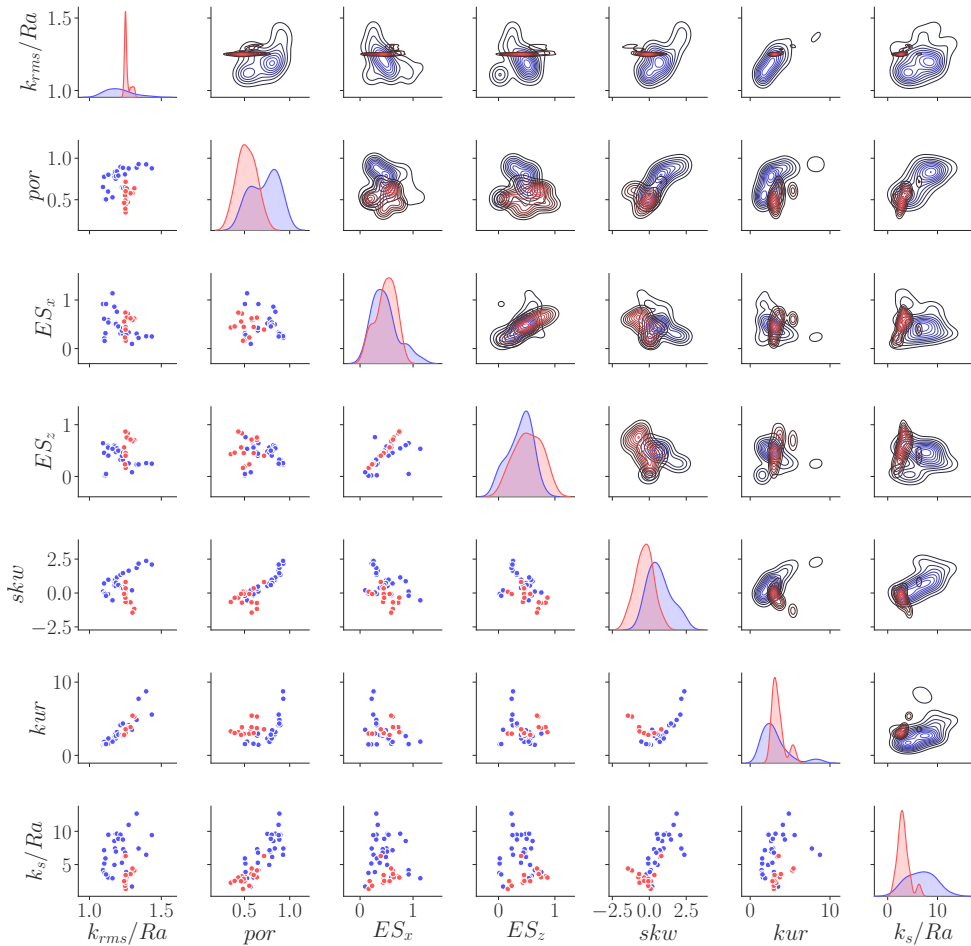


FIGURE 2. Pair plots of geometrical parameters and k_s , with k_s plots in the bottom row and the first column. DNS data (blue), experimental data (red).

$$por = \frac{1}{A_t k_c} \int_0^{k_c} A_f dy, \quad (2.11)$$

$$inc_x = \tan^{-1} \left\{ \frac{1}{2} skw \left(\frac{\partial k}{\partial x} \right) \right\}, \quad (2.12)$$

$$inc_z = \tan^{-1} \left\{ \frac{1}{2} skw \left(\frac{\partial k}{\partial z} \right) \right\}, \quad (2.13)$$

where $k(x, z)$ is the roughness height distribution and $A_f(y)$ and $A_t(y)$ are the fluid area and total area in (x, z) at each y plane. Although the surface geometries were generated using specialized shapes, these descriptive parameters are quite general and applicable to any rough surface. For all surfaces, $Ra/\delta \leq 0.04$, $k_c/\delta \leq 0.17$. The range of values of each parameter can be found in Figure 2.

2.3. Simulation parameters

Direct numerical simulation was used to calculate the pressure and velocity fields in turbulent open-channel flows over 45 different rough surfaces and one smooth one, at a fixed frictional Reynolds number $\text{Re}_\tau = 1000$. In these simulations, the domain sizes were $(L_x, L_y, L_z) = (3, 1, 1)\delta$, where δ is the channel half-height. The origin of the y axis is set at the elevation of the lowest trough for each rough surface. The number of grid points was $(n_x, n_y, n_z) = (400, 300, 160)$. A uniform mesh was used in the x and z directions, yielding grid sizes of $\Delta x^+ = 15.0$ and $\Delta z^+ = 12.5$, where $+$ denotes normalization in wall units. For all cases, the mesh in y was stretched with a hyperbolic tangent function from the wall onward. The first three y^+ grid points were located below 1. For the rough cases, at the roughness crest, $\Delta y/k_c \leq 0.017$ (with Case C11 giving the highest ratio). Here, k_c is the height of roughness crest measured from the lowest trough of a given surface. The maximum y grid size $\Delta y_{\text{max}}^+ = 19.0$ at channel center line (where the Kolmogorov length scale $\eta^+ \approx 6$). Moin & Mahesh (1998) provided arguments that the requirement to obtain reliable first- and second-order flow statistics is that the resolution be fine enough to accurately capture most of the dissipation. Moser & Moin (1987) noted that most of the dissipation in the curved channel occurs at scales greater than 15η (based on average dissipation). Existing DNS studies of channel and boundary layer flows that focus on these flow statistics typically use $\Delta x/\eta$ between 7 and 15 and $\Delta z/\eta$ between 4 and 8 (see, for examples, Kim *et al.* (1987), Spalart (1988) and Yuan & Piomelli (2014c)). The grid sizes herein satisfied $\Delta x/\eta < 7.5$, $\Delta y/\eta < 4.0$, and $\Delta z/\eta < 6.5$.

The spatial resolution of the roughness Taylor micro-scale, $\lambda_{T,x}$ in x and $\lambda_{T,z}$ in z , are used to evaluate the adequacy of the grid resolution to capture the roughness topographies, according to Yuan & Piomelli (2014b). The Taylor micro-scale is obtained by fitting a parabolic function to the two-point autocorrelation of the surface height fluctuations. It represents the size of an equivalent ‘roughness element’ in the context of random multiscale roughness. The streamwise and spanwise values of λ_T normalized by δ_ν and the respective grid size are tabulated in Table 2. For all cases, λ_{T,x_i}^+ are of orders 10 to 10^2 , indicating that average size of the roughness element is large compared to the viscous wall units. The average roughness elements are generally speaking resolved by the grid, with 4 to 12 grid points in each direction per λ_{T,x_i} , for most cases. Yuan & Piomelli (2014a) used a resolution of $\lambda_{T,x}/\Delta x \approx 4$ for the synthesized sand-grain surface (similar to Surface C43 herein) in a large-eddy simulation of channel flow. For some cases here, λ_T is not well resolved in at least one direction (with $\lambda_{T,x}/\Delta x$ or $\lambda_{T,z}/\Delta z$ less than 3). All these cases are among those that are not considered as fully-rough flows (the ones with $\hat{k}_s < 50$ discussed in the results section) and, consequently, not included in ML training and testing.

In rough wall flows, the pressure drag is caused primarily by the local flow structures and separation in the vicinity of individual roughness protuberances, which are predominately near-wall phenomena. To carry out the 46 separate DNS simulations for determining k_s efficiently, with sufficient near-wall resolution, we employ a small-span channel simulation approach. The concept of minimal-span simulation was introduced by Jimenez & Moin (1991). Chung *et al.* (2015) and MacDonald *et al.* (2017) carried out analyses of the performance of DNS over small spanwise domains for full and open channel flows on rough and smooth walls and showed that minimal-span simulations captured the essential near-wall dynamics and yielded accurate computations of wall friction, and of mean velocities and Reynolds stresses as far from the wall as $y \approx 0.3\delta$,

Case name	$\lambda_{T,x}^+$	$\lambda_{T,x}/\Delta x$	$\lambda_{T,z}^+$	$\lambda_{T,z}/\Delta z$
C01,r4,reg,inc1	19.7	2.6	21.1	3.4
C02,r4,reg,inc2	20.4	2.7	33.1	5.3
C03,r4,reg,inc3	19.8	2.6	22.9	3.7
C04,r6,reg,inc1	27.7	3.7	28.4	4.5
C05,r6,reg,inc2	31.6	4.2	39.1	6.2
C06,r6,reg,inc3	29.9	4.0	30.0	4.8
C07,r4,rnd,inc1	33.8	4.5	26.7	4.3
C08,r4,rnd,inc2	26.1	3.5	32.7	5.2
C09,r4,rnd,inc3	35.5	4.7	30.1	4.8
C10,r6,rnd,inc1	38.2	5.1	29.7	4.8
C11,r6,rnd,inc2	38.1	5.1	47.0	7.5
C12,r6,rnd,inc3	47.9	6.4	40.2	6.4
C13,r4,reg,por1	17.8	2.4	32.7	5.2
C14,r4,reg,por2	27.5	3.7	34.2	5.5
C15,r4,reg,por3	31.5	4.2	39.4	6.3
C16,r6,reg,por1	25.6	3.4	46.1	7.4
C17,r6,reg,por2	40.1	5.3	47.8	7.6
C18,r6,reg,por3	44.4	5.9	54.8	8.8
C19,r4,rnd,por1	32.7	4.4	31.1	5.0
C20,r4,rnd,por2	35.6	4.7	31.3	5.0
C21,r4,rnd,por3	37.4	5.0	34.2	5.5
C22,r6,rnd,por1	44.6	5.9	35.3	5.6
C23,r6,rnd,por2	47.1	6.3	39.7	6.4
C24,r6,rnd,por3	47.1	6.3	44.4	7.1
C25,r4,reg,ES1	89.0	11.9	–	–
C26,r4,reg,ES2	66.5	8.9	–	–
C27,r4,reg,ES3	27.1	3.6	–	–
C28,r6,reg,ES1	90.6	12.1	–	–
C29,r6,reg,ES2	66.8	8.9	–	–
C30,r6,reg,ES3	27.2	3.6	–	–
C31,r4,rnd,SGR	27.8	3.7	25.0	4.0
C32,r4,rnd,RND1	131.2	17.5	54.1	8.7
C33,r4,rnd,RND2	96.3	12.8	42.1	6.7
C34,r4,rnd,RND3	56.4	7.5	22.4	3.6
C35,r4,rnd,RND4	39.5	5.3	15.8	2.5
C36,r4,rnd,RND5	25.1	3.3	11.4	1.8
C37,r6,rnd,SGR	36.5	4.9	31.9	5.1
C38,r6,rnd,RND1	88.5	11.8	72.6	11.6
C39,r6,rnd,RND2	93.8	12.5	35.7	5.7
C40,r6,rnd,RND3	57.0	7.6	22.8	3.6
C41,r6,rnd,RND4	40.5	5.4	15.6	2.5
C42,r6,rnd,RND5	24.5	3.3	11.3	1.8
C43,SG	35.2	6.0	33.5	5.7
C44,TB	132.1	10.4	168.5	13.2
C45,CB	25.7	4.5	25.5	4.4

TABLE 2. Surface Taylor micro-scale, λ_T , in the streamwise and spanwise directions.

when the following constraints were met:

$$L_x \geq \max(1000\delta_\nu, 3L_z, \lambda_{r,x}), \quad (2.14a)$$

$$L_y \geq k_c/0.15, \quad (2.14b)$$

$$L_z \geq \max(100\delta_\nu, k_c/0.4, \lambda_{r,z}), \quad (2.14c)$$

where k_c is the roughness crest height, $\delta_\nu = \nu/u_\tau$, and λ_{r,x_i} is the characteristic

roughness wavelength in the x_i direction. The roughness Taylor microscale may be used as the characteristics wavelength; such length is much smaller compared to the domain size for all cases. Conditions (2.14a,c) were satisfied by choosing domain sizes L_x^+ and L_z^+ of 3000 and 1000 respectively. Condition (2.14b) is satisfied for all rough cases except for C11, which falls marginally below one constraint ($L_y = k_c/0.17$).

Periodic boundary condition were imposed in the streamwise and spanwise directions. No-slip and symmetry boundary conditions were imposed at the bottom and top boundaries respectively. When each simulation had reached statistical stationarity, statistics were collected over 5 large-eddy turn-over times (δ/u_τ). The time step $\Delta t^+ \leq 0.04$, orders of magnitude smaller than the time step required by DNS, as $\tau^+ \approx 0.2$, according to Choi & Moin (1994).

3. Results

3.1. Post-processed results

In Figure 3, the streamwise double-averaged velocity profiles computed in the present simulations are shown. The profiles in the logarithmic region are described for smooth- and rough-wall cases in the fully rough regime as:

$$\langle \bar{u} \rangle^+ = \frac{1}{\kappa} \ln(y^+) + 5.0, \quad \text{and} \quad (3.1a)$$

$$\langle \bar{u} \rangle^+ = \frac{1}{\kappa} \ln \left(\frac{y-d}{k_s} \right) + 8.5 \quad (3.1b)$$

respectively, where d is the zero-plane displacement, obtained as the location of the centroid of the wall-normal averaged drag-force profile (Jackson 1981). The shift in the y coordinate by d accounts for the flow blockage by surface roughness elements.

The values of d , thickness of the roughness sublayer y_R , bulk velocity U_b , wall friction coefficient $C_f = (u_\tau/U_b)^2$ are given in Table 3. y_R is defined as the location where $\langle \tilde{u}^2 \rangle^{1/2}$ reaches $0.06\langle \bar{u} \rangle$, similar to that proposed by Pokrajac *et al.* (2007).

To determine whether a particular flow is within the fully rough regime, Equation (3.1b) is applied to the computed logarithmic velocity profile to yield a test k_s value, denoted as \hat{k}_s . Its values for all cases are tabulated in Table 3. Cases with \hat{k}_s^+ greater than a threshold value of 50 are deemed to be in the fully rough regime (30 surfaces) and k_s is set to equal \hat{k}_s . Those below the threshold are considered transitionally rough (15 surfaces) and are not included in ML predictions in this study. The threshold value of k_s^+ —the lower end of the fully rough regime—has been observed to vary significantly for different types of roughness and is typically between 20 and 80.

The threshold value of k_s^+ which signifies the beginning of the fully rough regime is not determined more precisely because of the cost of carrying out, for each surface, simulations at successively higher values of k_s until the friction coefficient became invariant with Reynolds number. The uncertainty in k_s which might arise through treating all flows with $k_s^+ > 50$ as fully rough is partially compensated for by incorporating an assumed 10 % noise level in the learning stage of the GPR prediction of k_s .

In Figure 2, the pair plots of the different topographic roughness parameters are shown as scatter plots (lower right), joint pdfs (upper left), and distribution pdfs (diagonal). Pair scatter plots for the true (DNS and experimental) value of k_s and other roughness parameters are shown in the bottom row of this figure. It can be seen that, for the roughness cases chosen, there is some correlation between kurtosis and rms roughness (column 1, row 6) and kurtosis and skewness (column 5, row 6) though the relationship

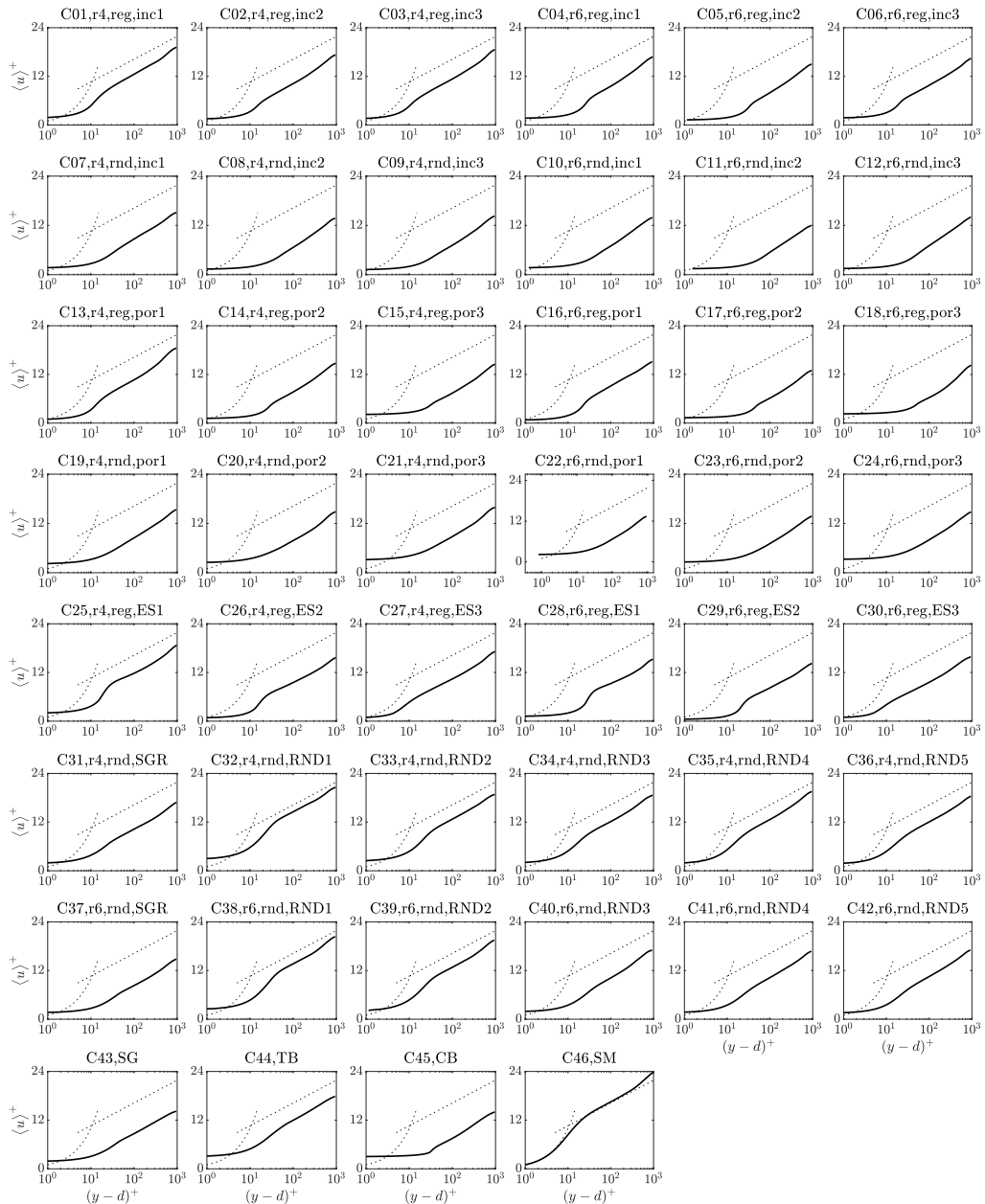


FIGURE 3. Profiles of streamwise double-averaged velocity plotted against a zero-plane-displacement shifted logarithmic y abscissa. The dashed lines are $u^+ = y^+$ and $2.5 \ln(y-d)^+ + 5.0$.

between others appears to be more random. From the graphs in the bottom row, it can be seen that k_s/Ra scales on porosity to some power, albeit with some scatter (column 2, row 7). It also appears that k_s/Ra might decrease with skewness for surfaces with $skw < 0$ and increase with skewness in cases with $skw > 0$ (column 5, row 7). Surfaces with positive skewness yields higher k_s compared to those with negative skewness, consistent with observation of Flack *et al.* (2019). Beyond these observations, there does not appear

Case name	d/δ	y_R/δ	\widehat{k}_s^+	U_b	C'_f
C01,r4,reg,inc1	0.032	0.074	19.4	15.7	4.1
C02,r4,reg,inc2	0.046	0.074	49.7	13.5	5.5
C03,r4,reg,inc3	0.033	0.071	31.0	14.8	4.6
C04,r6,reg,inc1	0.038	0.088	64.4	13.2	5.7
C05,r6,reg,inc2	0.057	0.114	124.4	11.3	7.8
C06,r6,reg,inc3	0.045	0.075	58.9	12.8	6.1
C07,r4,rnd,inc1	0.044	0.465	93.9	11.8	7.2
C08,r4,rnd,inc2	0.058	0.420	216.9	10.1	9.8
C09,r4,rnd,inc3	0.043	0.182	173.9	10.7	8.7
C10,r6,rnd,inc1	0.062	0.300	187.7	10.3	9.3
C11,r6,rnd,inc2	0.081	0.572	353.7	8.5	13.8
C12,r6,rnd,inc3	0.055	0.178	184.7	10.4	9.2
C13,r4,reg,por1	0.047	0.069	41.4	14.3	4.9
C14,r4,reg,por2	0.032	0.367	140.6	11.3	7.8
C15,r4,reg,por3	0.028	0.086	157.1	11.1	8.1
C16,r6,reg,por1	0.066	0.549	76.7	11.6	7.5
C17,r6,reg,por2	0.044	0.492	259.8	9.6	10.7
C18,r6,reg,por3	0.039	0.144	246.5	10.4	9.3
C19,r4,rnd,por1	0.048	0.127	101.6	11.7	7.3
C20,r4,rnd,por2	0.037	0.285	132.2	11.4	7.8
C21,r4,rnd,por3	0.027	0.112	88.5	12.5	6.4
C22,r6,rnd,por1	0.069	0.263	211.9	9.8	10.4
C23,r6,rnd,por2	0.047	0.350	177.3	10.5	9.1
C24,r6,rnd,por3	0.040	0.281	123.0	11.5	7.6
C25,r4,reg,ES1	0.023	0.049	25.6	15.1	4.4
C26,r4,reg,ES2	0.026	0.350	65.3	12.5	6.4
C27,r4,reg,ES3	0.035	0.356	45.5	13.6	5.4
C28,r6,reg,ES1	0.033	0.304	71.2	12.0	6.9
C29,r6,reg,ES2	0.040	0.432	112.0	11.0	8.2
C30,r6,reg,ES3	0.054	0.238	64.0	12.5	6.4
C31,r4,rnd,SGR	0.032	0.069	48.7	13.4	5.6
C32,r4,rnd,RND1	0.041	0.000	8.4	17.2	3.4
C33,r4,rnd,RND2	0.043	0.102	17.6	15.5	4.2
C34,r4,rnd,RND3	0.045	0.102	22.5	15.1	4.4
C35,r4,rnd,RND4	0.046	0.072	18.3	15.7	4.1
C36,r4,rnd,RND5	0.051	0.309	23.4	14.7	4.6
C37,r6,rnd,SGR	0.046	0.234	108.8	11.4	7.7
C38,r6,rnd,RND1	0.060	0.112	12.0	16.3	3.8
C39,r6,rnd,RND2	0.062	0.108	17.1	15.4	4.2
C40,r6,rnd,RND3	0.070	0.137	50.4	13.1	5.8
C41,r6,rnd,RND4	0.073	0.340	48.7	12.8	6.1
C42,r6,rnd,RND5	0.076	0.018	43.8	13.0	5.9
C43,SG	0.044	0.472	93.0	11.4	7.7
C44,TB	0.058	0.149	24.1	14.6	4.7
C45,CB	0.039	0.106	149.9	11.0	8.3
C46,SM	0.000	0.011	0.0	20.4	2.4

TABLE 3. Flow-related parameters obtained from DNS. Here, $C'_f = C_f \times 10^3$. The flow is assumed fully rough if $\widehat{k}_s^+ \gtrsim 50$; in this case, k_s is set to equal to \widehat{k}_s .

to be a clear linear correlation between k_s and any individual roughness parameter, which makes the search for a functional dependence of k_s on these parameters a problem well suited to ML.

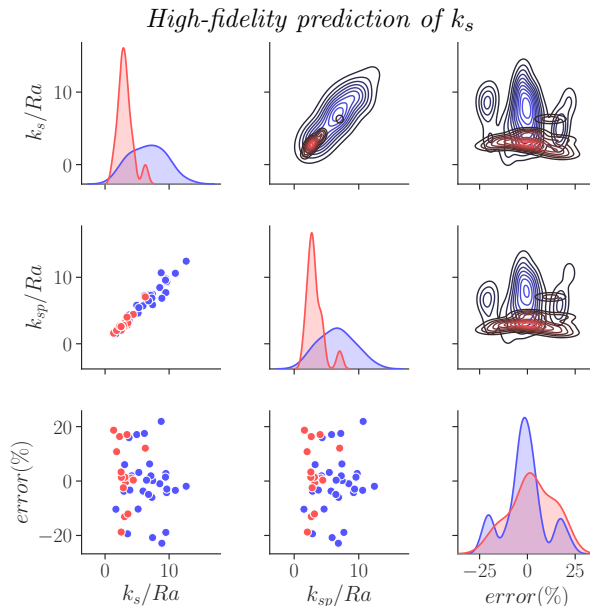


FIGURE 4. Pair plots of true k_s , predicted k_s (denoted as k_{sp}) and the relative error. DNN method. DNS data (*blue*), experimental data (*red*).

3.2. ML predictions of the equivalent sand-grain height

The ML techniques of Deep Neural Networks and Gaussian Process Regression were employed to predict k_s from the data sets described in the previous section. Their main characteristics are described below:

- The neural network architecture chosen was a *Multi Layer Perceptron*, with three hidden layers. The activation functions on all nodes were of the *Rectified Linear Unit* kind, and kernel regularization was used to avoid overfitting. The network had 730 trainable weights in total. This architecture was found to provide suitable accuracy in modeling without overfitting, for this particular multivariate labeled regression problem.

- The Gaussian Process Regression used *Rational Quadratic* kernels, and incorporated an assumed 10% noise level in the learning stage, for reasons explained in the preceding section.

- The data set was split randomly into two groups—one comprising 70% of the data sets and the other 30%—for the respective training and testing processes.

- The database consisted of DNS of turbulent channel flows over 30 different surfaces at $Re_\tau = 1000$, and the results of 15 experimental data sets. All data were believed to correspond to the fully rough turbulent flow regime.

- The inputs for both techniques were 17 roughness geometrical parameters, 8 of which were primary variables defined in Equations (2.6) to (2.13). The other 9 were products of the primary variables, which were added to improve the efficiency of each learning stage. These were products of ES_x with all other primary variables, as well as $(k_{rms})(skw)$ and $(kur)(skw)$. We chose these products owing to the existing knowledge of the importance of these parameters for certain types of roughness.

The predictions of k_s , henceforth called k_{sp} , are shown as pair plots in Figures 4 and 5, for the DNN and GPR methods respectively. Scatter plots of the equivalent sand-grain height k_{sp} predicted from the surface topography parameters and the true value of k_s (column 1, row 2) reveal a tight clustering of data along the $y = x$ diagonal, with only a

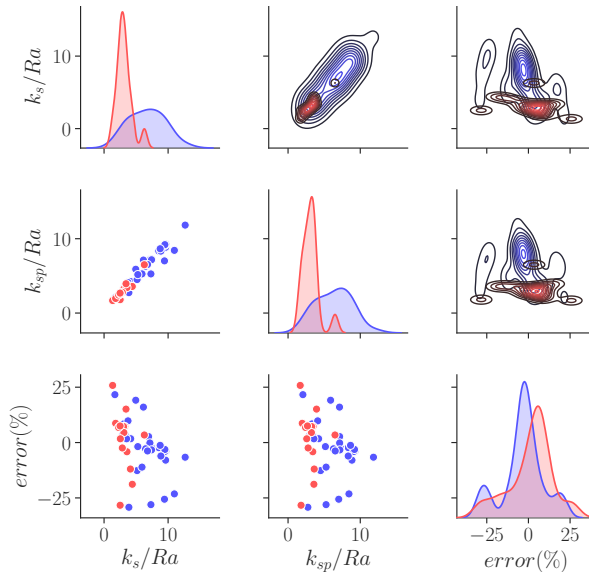


FIGURE 5. Pair plots of true k_s , predicted k_s (denoted as k_{sp}) and the relative error. GPR method. DNS data (*blue*), experimental data (*red*).

few outlying points, in both figures. This very high degree of correlation between k_{sp} and k_s implies that both techniques have been applied with equal success to this prediction problem. The error range (column 1, row 3) is less than $\pm 25\%$ for each technique. It is possible that smaller error ranges might be achieved if important roughness parameters have been omitted from the inputs, if more favorable algebraic combinations of the present choice of input parameters were not explored in the two prediction techniques considered, or if more sophisticated ML techniques had been applied. However, the consistency between both the k_s predictions and error bands for two quite different ML techniques suggests that they are both well-suited to this kind of problem, and possibly close to an optimum for this class of ML approach.

The error values (in percent) for the DNN and GPR methods is given in Table 4, together with the error of the empirical relation

$$k_s = 2.91k_{rms}(2 + skw)^{-0.284} \quad (3.2)$$

proposed by Flack *et al.* (2016), which is used as a base empirical relation in our study to compare with. For the DNS data set, only the fully-rough cases are compared. Note the errors associated with Equation (3.2) are small for surfaces with index E-16 as they were used to calibrate this relation. It is evident that the error reaches as large as 120% for Equation (3.2), owing to the small number of training data and geometrical variables used in the calibration of Equation (3.2).

3.3. Uncertainty estimation

The GPR method provides confidence margins for its prediction of equivalent sand-grain height, as functions of each input parameter. These margins can be very useful for indicating the kinds of surfaces for which additional training data could improve the confidence in predictions. This feature of the GPR approach makes it very attractive for studies of this kind, since DNS and experimental generation of data is expensive.

The confidence intervals determined by the GPR technique are shown as functions of

Case name	err_{DNN}	err_{GPR}	err_{base}
C04,r6,reg,inc1	-0.0	3.3	-16.2
C05,r6,reg,inc2	1.9	1.7	-38.1
C06,r6,reg,inc3	6.0	8.4	-10.6
C07,r4,rnd,inc1	17.1	19.1	-47.1
C08,r4,rnd,inc2	-1.0	-2.3	-70.4
C09,r4,rnd,inc3	-4.3	-8.0	-72.5
C10,r6,rnd,inc1	0.2	-2.4	-66.1
C11,r6,rnd,inc2	-3.0	-4.0	-74.1
C12,r6,rnd,inc3	6.3	2.7	-62.9
C14,r4,reg,por2	1.9	-0.2	-66.3
C15,r4,reg,por3	-3.4	-23.2	-76.6
C16,r6,reg,por1	-3.8	3.6	3.1
C17,r6,reg,por2	-18.9	-4.0	-74.6
C18,r6,reg,por3	-1.9	-6.6	-79.2
C19,r4,rnd,por1	17.5	16.0	-55.6
C20,r4,rnd,por2	2.8	-3.1	-73.6
C21,r4,rnd,por3	-20.8	-3.3	-64.9
C22,r6,rnd,por1	-22.9	-6.1	-69.9
C23,r6,rnd,por2	21.9	-1.3	-71.2
C24,r6,rnd,por3	0.3	-2.8	-58.8
C26,r4,reg,ES2	-10.3	-12.7	-48.4
C28,r6,reg,ES1	15.9	9.8	-29.0
C29,r6,reg,ES2	-3.7	-11.1	-54.7
C30,r6,reg,ES3	-19.4	1.7	-21.8
C31,r4,rnd,SGR	3.2	-1.8	-47.1
C37,r6,rnd,SGR	-6.0	-28.0	-61.3
C40,r6,rnd,RND3	-3.3	-29.2	-23.0
C43,SG	-4.9	-3.8	-58.6
C44,TB	-10.4	21.6	78.3
C45,CB	1.4	-25.6	-70.4
E01,16,2	-0.4	7.3	6.2
E02,16,3	-13.1	7.2	3.3
E03,16,7	1.1	-12.0	-2.2
E04,16,8	0.3	-18.8	1.3
E05,16,9	1.4	4.5	10.9
E06,16,15	-12.1	-4.2	-3.0
E07,18,1	-18.8	-28.3	17.3
E08,18,2	18.7	25.8	120.7
E09,19,1	10.8	8.7	66.8
E10,19,2	-2.5	-2.4	5.8
E11,19,3	16.3	6.8	47.4
E12,19,4	1.4	1.7	24.1
E13,19,5	17.1	15.1	-16.6
E14,19,6	12.1	3.4	-56.8
E15,19,7	3.3	7.5	19.8

TABLE 4. Actual errors in k_s prediction for DNN, GPR, compared to err_{base} , errors of the base empirical correlation (Flack *et al.* 2016) of $k_s = 2.91k_{rms}(2 + skw)^{-0.284}$. The errors are in percent.

the normalized surface rms roughness height, effective slope, porosity and skewness in Figure 6. Wider intervals indicate higher estimated values of predictive error, such as at roughness porosity of 0.45, and skewnesses of -1.2 and 1.7. Surfaces with roughness with these statistical properties are then priorities for further simulations and experiments.

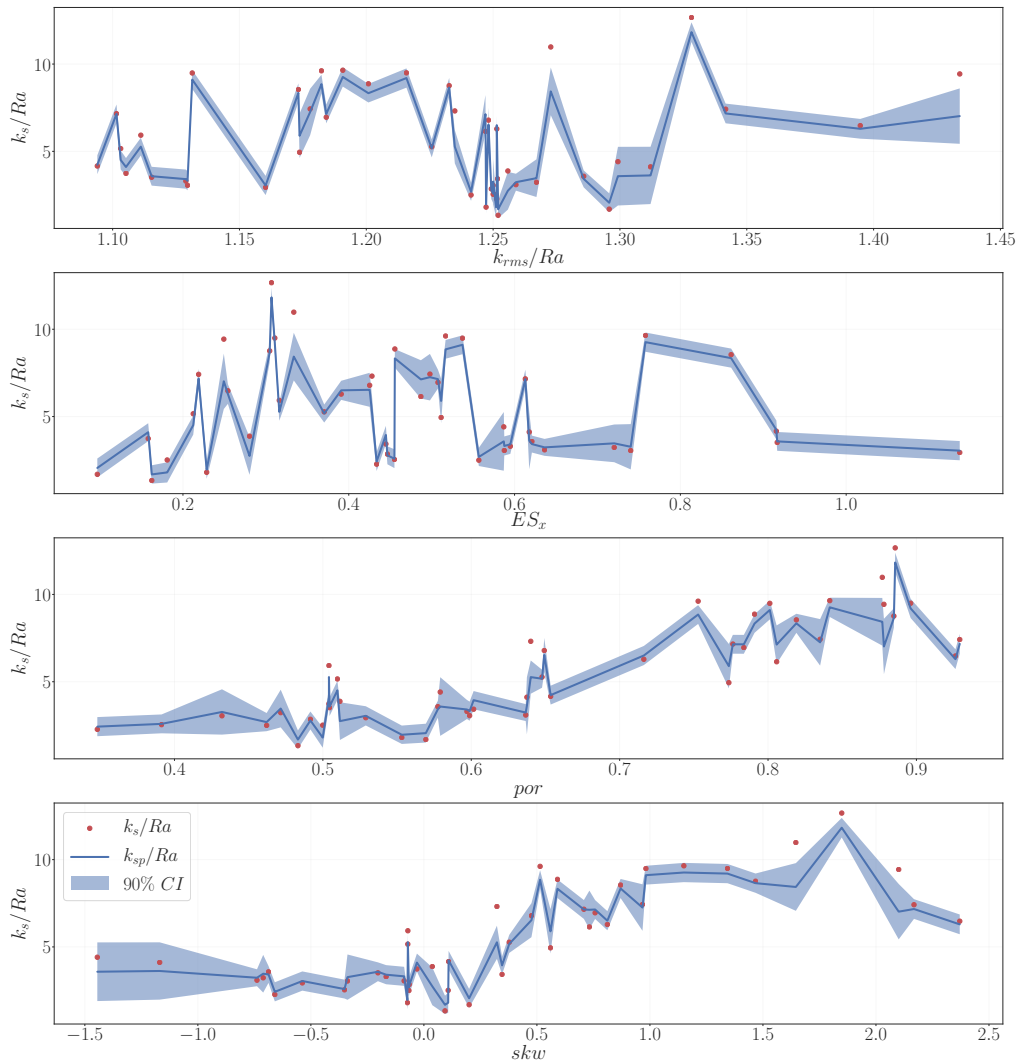


FIGURE 6. Confidence interval of prediction obtained from GPR method. Predicted k_s/Ra in blue lines and true k_s/Ra in red dots.

4. Concluding remarks

The equivalent sand-grain height k_s of a rough surface appears to depend on many geometrical parameters. Consequently, methods of prediction based on a subset of only a few parameters have a very limited ability to predict k_s and such predictions can have large deviations from the true value of k_s . While this limitation can be addressed by including more surface-descriptive parameters, it also increases the complexity of the regression procedure needed to determine the predictive model. Machine learning techniques, which can easily handle large multi-parameters problems, can be employed to both predict k_s from multiple inputs and systematically analyze the effect of different geometrical parameters on the prediction. In this paper, we presented a Deep Neural Network and a Gaussian Process Regressor that were shown to be capable of predicting

k_s with $err_{rms} < 10\%$ and $err_{max} < 30\%$, which is significantly better than predictions based on conventional analyses. We therefore conclude that these machine learning techniques offer high-fidelity predictions of the equivalent sand-grain roughness height for turbulent flows over a wide range of rough surfaces. These methods are likely to enjoy similar success in related multi-parameter labeled regression problems.

The machine learning approaches described here are essentially black box techniques, in which the output is a series of weights, or their equivalent, applied at nodes of a network. While such black box techniques appear to provide efficient and accurate predictions, given a suitable set of training data, they provide little insight into the underlying physical processes, which are usually of great importance for the purposes of design, or extrapolation of predictions beyond the training data. The related problem of deducing a white box model which approximates the predictive capabilities of the black box one, and would reveal information on the features of surface roughness which contribute most to the determination of the hydrodynamic roughness height k_s is a more challenging one, and is a topic for future work.

5. Acknowledgements

The authors gratefully acknowledge the Office of Naval Research for the financial support of this research (Award No. N00014-17-1-2102). Computational support was supplied by Michigan State University through computational resources provided by the Institute for Cyber-Enabled Research.

REFERENCES

- AGHAEI JOUYBARI, M., BRERETON, G.J. & YUAN, J. 2019 Turbulence structures over realistic and synthetic wall roughness in open channel flow at $re_\tau = 1000$. *Journal of Turbulence* **20** (11-12), 723–749, arXiv: <https://doi.org/10.1080/14685248.2019.1706741>.
- BARROS, J. M., SCHULTZ, M. P. & FLACK, K. A. 2018 Measurements of skin-friction of systematically generated surface roughness. *Int. J. Heat Fluid Flow* **72**, 1–7.
- BONS, J. P. 2002 St and c_f augmentation for real turbine roughness with elevated freestream turbulence. *J. Turbomach.* **124**, 632–644.
- BONS, J. P., TAYLOR, R. P., MCCLAIN, S. T. & RIVIR, R. B. 2001 The many faces of turbine surface roughness. *J. Turbomach.* **123**, 739–748.
- CHOI, H. & MOIN, P. 1994 Effects of the computational time step on numerical solutions of turbulent flow. *J. Comput. Phys.* **113**, 1–4.
- CHUNG, D., CHAN, L., MACDONALD, M., HUTCHINS, N. & OOI, A. 2015 A fast direct numerical simulation method for characterising hydraulic roughness. *J. Fluid Mech.* .
- FLACK, K. A. 2018 Moving beyond moody. *J. Fluid Mech.* **842**, 1–4.
- FLACK, K. A. & SCHULTZ, M. P. 2010 Review of hydraulic roughness scales in the fully rough regime. *J. Fluids Eng.* **132**, 041203–1–10.
- FLACK, K. A., SCHULTZ, M. P. & BARROS, J. M. 2019 Skin friction measurements of systematically-varied roughness: Probing the role of roughness amplitude and skewness. *Flow, Turbul. Combust.* pp. 1–13.
- FLACK, K. A., SCHULTZ, M. P., BARROS, J. M. & KIM, Y. C. 2016 Skin-friction behavior in the transitionally-rough regime. *Int. J. Heat Fluid Flow* **61**, 21–30.
- GÉRON, AURÉLIEN 2017 *Hands-on machine learning with Scikit-Learn and TensorFlow: concepts, tools, and techniques to build intelligent systems.* ” O’Reilly Media, Inc.”.
- JACKSON, P. S. 1981 On the displacement height in the logarithmic velocity profile. *J. Fluid Mech.* **111**, 15–25.
- JIMÉNEZ, J. 2004 Turbulent flows over rough walls. *Annu. Rev. Fluid Mech.* **36**, 173–196.
- JIMENEZ, J. & MOIN, P. 1991 The minimal flow unit in near-wall turbulence. *J. Fluid Mech.* **225**, 213–240.

- KEATING, A. 2004 Large-eddy simulation of heat transfer in turbulent channel flow and in the turbulent flow downstream of a backward-facing step. PhD thesis, University of Queensland.
- KIM, J., MOIN, P. & MOSER, R. D. 1987 Turbulence statistics in fully developed channel flow at low Reynolds number. *J. Fluid Mech.* **177**, 133–166.
- LECUN, YANN, BENGIO, YOSHUA & HINTON, GEOFFREY 2015 Deep learning. *nature* **521** (7553), 436.
- MACDONALD, M., CHUNG, D., HUTCHINS, N., CHAN, L., OOI, A. & GARCÍA-MAYORAL, R. 2017 The minimal-span channel for rough-wall turbulent flows. *J. Fluid Mech.* **816**, 5–42.
- MOIN, P. & MAHESH, K. 1998 Direct numerical simulation: a tool in turbulence research. *Annu. Rev. Fluid Mech.* **30** (1), 539–578.
- MOSER, R. D. & MOIN, P. 1987 The effects of curvature in wall-bounded turbulent flows. *J. Fluid Mech.* **175**, 479–510.
- NAPOLI, E., ARMENIO, V. & DE MARCHIS, M. 2008 The effect of the slope of irregularly distributed roughness elements on turbulent wall-bounded flows. *J. Fluid Mech.* **613**, 385–394.
- NIKURADSE, J. 1933 Laws of flow in rough pipes. *NACA Technical Memorandum 1292*.
- POKRAJAC, D., CAMPBELL, L. J., NIKORA, V. & MANES, C. ADN MCEWAN, I. 2007 Quadrant analysis of persistent spatial velocity perturbations over square-bar roughness. *Exp. Fluids* **42**, 413–423.
- RAUPACH, M. R., ANTONIA, R. A. & RAJAGOPALAN, S. 1991 Rough-wall boundary layers. *Appl. Mech. Rev.* **44**, 1–25.
- RAUPACH, M. R. & SHAW, R. H. 1982 Averaging procedures for flow within vegetation canopies. *Bound.-Lay. Meteorol.* **22**, 79–90.
- VAN RIJ, J. A., BELNAP, B. J. & LIGRANI, P. M. 2002 Analysis and experiments on three-dimensional, irregular surface roughness. *J. Fluids Eng.* **124**, 671–677.
- SCHULTZ, M. P. & FLACK, K. A. 2009 Turbulent boundary layers on a systematically varied rough wall. *Phys. Fluids* **21**, 015104–1–9.
- SCOTTI, A. 2006 Direct numerical simulation of turbulent channel flows with boundary roughened with virtual sandpaper. *Phys. Fluids* **18**, 031701–1–4.
- SPALART, P. R. 1988 Direct simulation of a turbulent boundary layer up to $R_\theta = 1410$. *J. Fluid Mech.* **187**, 61–98.
- YUAN, J. & PIOMELLI, U. 2014a Estimation and prediction of the roughness function on realistic surfaces. *J. Turbul.* **15**, 350–365.
- YUAN, J. & PIOMELLI, U. 2014b Numerical simulations of sink-flow boundary layers over rough surfaces. *Phys. Fluids* **26**, 015113–1–015113–28.
- YUAN, J. & PIOMELLI, U. 2014c Roughness effects on the reynolds stress budgets in near-wall turbulence. *J. Fluid Mech.* **760**, R1.